Nanoscale

PAPER

Cite this: *Nanoscale*, 2019, **11**, 2521

A platform for nanomagnetism – assembled ferromagnetic and antiferromagnetic dipolar tubes†

Igor Stanković, *[a] Miljan Dašić,[a] Jorge A. Otálora[b] and Carlos García[c]

Received 27th August 2018,
Accepted 25th November 2018

DOI: 10.1039/c8nr06936k

rsc.li/nanoscale

We report an interesting case where magnetic phenomena can transcend mesoscopic scales. Our system consists of tubes created by the assembly of dipolar spheres. The cylindrical topology results in the breakup of degeneracy observed in planar square and triangular packings. As far as the ground state is concerned, the tubes switch from circular to axial magnetization with increasing tube length. All magnetostatic properties found in magnetic nanotubes, in which the dipolar interaction is comparable to or dominant over the exchange interaction, are reproduced by the dipolar tubes including an intermediary helically magnetized state. Besides, we discuss the antiferromagnetic phase resulting from the square arrangement of the dipolar spheres and its interesting vortex state.

1. Introduction

Whether a system behaves as classical or quantum is usually determined by the ratio between its spatial dimension and quantum coherence length. Even so, there are cases where the actual size dependent behavior seems to be an illusion and transcending the scales is possible, thus allowing the study of fundamental aspects hardly accessible at the original size. Spin-ice frustration[1–4] is an example, wherein the micro- and mesoscopic rules that govern the spin orientation of such systems can become very subtle and hard to understand. Nevertheless, Venderbos *et al.*[5] and Mellado *et al.*[6] have shown that similar frustrated states can also arise in arrangements of macroscopic dipolar rotors *via* classical magnetic interactions, furthermore, showing phenomena that are not visible in their microscopic counterpart. In this paper, we present a similar scenario of scale transcendence, relating magnetic nanotubes (MNTs) to self-assembled dipolar magnetic spheres arranged in tubular structures, named here *dipolar tubes*. The spheres can have radii from 10 nm to macroscopic neodymium balls. A peculiar feature of this comparison is that the tubular geometry of dipolar tubes breaks-up the continuous degeneracy of the ground states in the two dimensional (2D) lattices of dipolar spheres.[7,8] As a result, we expect a number of new stable states in the tubular geometry. The curvature-induced feature opens the inquiry on its impact on the energy barriers that separate and stabilize the novel magnetic states, which will be addressed in this manuscript.

Given the lack of exchange interaction in dipolar tubes, it is most reasonable to compare them with dipolar interaction dominated MNTs where the exchange interaction is negligible. Since in MNTs the dipolar interaction dominated state is *circular* (magnetization polarized azimuthally), it can be expected that transcendence exists only with a similar circular state in dipolar tubes. As we show in the manuscript, it is found that the scale transcendence strikingly goes beyond this trivialization. In a ground state, the stray field created by MNTs should be minimal. This condition stems from micromagnetic considerations[9–11] wherein the magnetostatic energy is minimized due to the dipolar part of the energy. Apart from the circular state, *axial* and *helical* ground states in MNTs have been predicted theoretically[12,13] ‡ and confirmed experimentally.[14–18] In the axial state, the magnetization is parallel to the nanotube's axis in the center of the tube and gradually turns into circular magnetization at the nanotube ends. In the helical state, the magnetization is never completely aligned with the tube's axis resulting in a circulating component of the magnetization.[12,13] The helical and axial states spontaneously

[a]*Scientific Computing Laboratory, Center for the Study of Complex Systems, Institute of Physics Belgrade, University of Belgrade, 11080 Belgrade, Serbia. E-mail: igor.stankovic@ipb.ac.rs*

[b]*Departamento de Física & Centro Científico Tecnológico de Valparaíso-CCTVal, Universidad Técnica Federico Santa María, Av. España 1680, Casilla 110-V, Valparaíso, Chile*

[c]*Institute for Metallic Materials at the Leibniz Institute for Solid State and Materials Research, IFW, 01069 Dresden, Germany*

†Electronic supplementary information (ESI) available. See DOI: 10.1039/C8NR06936K

‡Elsewhere in the literature the axial state is also referred to as mixed and helical as the transition state, *cf.* ref. 13. In this work, we chose to name the states based on magnetization in the center of the tube.

emerge when the dipolar interaction is comparable to the exchange interaction. Both states occur when nanotube's radius is a few tens of times larger than the exchange length. The axial state appears when the MNT length is around two to three orders of magnitude larger than its diameter, whereas the helical state is a transition configuration to the circular state that appears when the length of the tube is further reduced. Most of the previous studies on magnetic nanotubes have focused on magnetic configurations as a function of geometry for specific material parameters. Only recently Salinas *et al.*[19] applied a generic model to discover that helical phases possess a high level of metastability relevant to magnetization reversal modes. Still, the origin of small energy differences between the states remained unclear. The axial and helical states create a small stray field[13] or exponential decaying in the case of infinite structures, and therefore they could also exist in dipolar tubes.[20]

The cylindrical magnetic geometry of MNTs has advantages for applications despite evident fabrication problems. In fact, the elongated geometry, azimuthal symmetry, and curvature of nanotubes bring reproducibility, robustness, and extra stability to nanotube's equilibrium states and magnetization dynamics,[12,13,21–25] which makes MNTs attractive for buffering, transport and processing information using their equilibrium states, and domain wall dynamic and spin-wave excitations. In this sense, the proper understanding and characterization of equilibrium states in MNTs is, thus, a mandatory task. Under this scenario, mimicking the magnetic equilibrium features of nanotubes with dipolar tubes can facilitate and encourage developments towards alternative techniques intended to reduce the complexity of experiments. The minimal energy structures of dipolar particles have been investigated in recent theoretical studies.[26,27] The tubular form of the ground state together with outstanding self-assembly properties of dipolar particles[28,29] present motivation for their application as a platform for testing concepts with MNTs. For instance in experiments, tubular and helical architectures with dipolar particles were obtained *via* DNA ligations,[30,31] confinement,[32–34] bulk interactions – magnetic Janus colloids,[35] and asymmetric colloidal magnetic dumbbells.[36] Another interesting system with respect to magnetic order is the two dimensional self-assembled super lattices of magnetic cubes. The magnetic cubes are synthesized with two most probable orientations: axial [001][37] and along the principal diagonal of the crystal, *i.e.*, cube, [111],[38] but the possibility of less trivial orientations should not be discounted. As a result of the interplay of square packing and magnetization defined by their crystal structure, we find axially magnetized anti-ferromagnetic states in the case of [001] and *vortex* in the case of [111] magnetized cubes.[39,40] At this point, we would like to draw attention to two recently developed techniques with which dipolar tubes could be realised: (i) two-photon lithography[41] nano-printers can fabricate complex three-dimensional structures with the resolution of up to 300 nm. The two-photon lithography technique was used to fabricate nanostructures out of polymer, metallic,[42] and recently magnetic[43] materials. Such printed structures could be used as a template for the self-assembly of magnetic particles with rhombic and square lattices. (ii) The second technique comes from micro-fluidics. The tubular structures of magnetic particles can be created by the conformal covering of the cylindrical conductive wire surface by assisting the self-ordering process of magnetic microspheres[44] *via* the application of a circular electromagnetic field induced by an injected electrical current along the wire.

With the aim of addressing our results, linking self-assembly, geometry, and magnetization states in dipolar tubes, this paper is organized as follows: section 2 introduces the dipolar interaction model and methods used. We discuss self-organization on cylindrical confinement in section 3, and *in silico* hierarchical degeneracy breakup of the infinite square and triangular lattices with an introduction of curvature in section 4. We also present a systematic study of the ground state configurations and energies resulting from the interplay between the tube's length and curvature for triangular and square arrangements in section 4. The final section, section 5, gives the conclusion and outlook.

2. Models and methods

2.1. Magnetic interaction model

Magnetic nanoparticles can have complex coupling involving both dipolar and exchange interactions. The atomic exchange interaction is relevant up to a length scale of 10 nm.[45] Thus, dipolar coupling dominates in the formation of the structures on the length scales 10 nm–100 μm, with many potential applications.[30–35] We characterize the system using dipole–dipole interaction potential: it is assumed that each particle carries identical dipolar (magnetic) moment with magnitude $m = |\vec{m}_i|$, where $\vec{m}_i = (m_i{}^x, m_i{}^y, m_i{}^z)$ defines the dipolar moment of particle i. The potential energy of interaction $U(\vec{r}_{ij})$ between two point-like dipoles with centers located at $\vec{r}_i$ and $\vec{r}_j$ can be written as:

$$U(\vec{r}_{ij}) = \frac{\mu_0}{4\pi}\left[\frac{\vec{m}_i \cdot \vec{m}_j}{{r_{ij}}^3} - 3\frac{(\vec{m}_i \cdot \vec{r}_{ij})(\vec{m}_j \cdot \vec{r}_{ij})}{{r_{ij}}^5}\right], \quad (1)$$

for $r_{ij} \geq d$ or ∞ otherwise, where $r_{ij} = |\vec{r}_{ij}| = |\vec{r}_j - \vec{r}_i|$ and d is particle's diameter. It is convenient to introduce the energy scale defined by $U_{\uparrow\uparrow} \equiv \mu_0 m^2/4\pi d^3$ that physically represents the repulsive potential value for two parallel dipoles in contact standing side by side, as clearly suggested by the notation. Thereby, the total potential energy of interaction in a given structure U_{tot} is given by

$$U_{\mathrm{tot}} = \sum_{i>j} U(\vec{r}_{ij}). \quad (2)$$

One can then define the reduced potential energy of interaction u (per particle) of N magnetic spheres. It reads:

$$u_N = \frac{U_{\mathrm{tot}}}{U_{\uparrow\uparrow} N}, \quad (3)$$

which will be referred to as the *cohesive energy*. The cohesive energy of a particle is directly related to the energy required to take it out from the structure. Lower cohesive energy means it

takes more energy to disintegrate the structure. The higher is the absolute value of cohesive energy the more stable is the structure. For a particular two particle head-to-tail configuration (*i.e.*, →→), we get $u_2 = -1$ per particle.

There is significant flexibility in tuning the physical and chemical properties of magnetic particles. In particular, colloids can be synthesized either from a pure magnetic material like hematite with a small spontaneous magnetization ($I^s_{FeO} \approx 2.2$ kA m^{-1}), or large in the case of magnetite or cobalt ferrite ($I^s_{CoFe} \approx 480$ kA m^{-1}).[46,47] In the case of core–shell particles, a design freedom is obtained by the adjustable core to shell ratio. Here, in particular, we consider that all magnetic particles have the same magnetic moment. We assume that the particles are silica–hematite core–shell particles with outer diameter $d = 50$ μm and hematite core $d_{core} = 10$ μm.[48] Assuming a single domain particle behavior, the magnetic moment m is expressed as $m = I^s_{FeO} v = 1.15$ A μm^2, where $v \approx 500$ μm^3 is the volume of the magnetic part of the particle. The result in this work should be independent on the particle material or size. To facilitate comparison, we present results in the scaled units with the reference magnetic interaction energy $U_{\uparrow\uparrow} = 10^{-18}$ J calculated for hematite core/shell particles. For reference energy we take the minimum of magnetic cohesive energy of two particles in contact. The reference magnetic energy $U_{\uparrow\uparrow}$ is therefore equal to $256k_BT$, where $T = 300$ K is the temperature and k_B is the Boltzmann's constant. The maximal magnetic field generated by one particle at the center of the mass of the other particle (placed side by side) is $B_0 = \mu_0 m/(2\pi d^3) = 1$ μT. The size of the magnetic core has a strong influence on the energy scale: for $d_{core} = 20$ μm, we would obtain magnetic moment $m = I^s_{FeO} v = 9.2$ A μm^2, and magnetic energy depends on the square of magnetic moment $U_{\uparrow\uparrow} = 67 \times 10^{-18}$ J, *i.e.*, $1.6 \times 10^4 k_BT$. As a result, one could tune the level of degeneracy described in latter sections with the size of the core. Also, by changing the core to shell ratio we tune the balance of interaction between particles and of particles with the field created by a conducting wire.

2.2. Isotropic interaction

When the dipolar coupling is strong, such as in nanocrystals, the particle assembly is determined unequivocally by the dipolar coupling and the particle shape. Here, we are interested in moderately interacting magnetic particles since we want to avoid the spontaneous formation of the clusters. Self-assembly requires to take advantage of forces that dominate on the micron scale and below (magnetic, contact, and van der Waals), resulting in different device designs and functionalities.[49]

We describe the effect of isotropic contact and van der Waals interactions between the spherical particles using a minimal model, *i.e.*, as soft-core beads, that interact isotropically by means of a truncated and shifted Lennard-Jones potential. The interaction is defined as: $U^{cut}_{LJ}(r) = U_{LJ}(r) - U_{LJ}(r_{cut})$, $r < r_{cut}$ and $U_{cut} = 0$, $r \geq r_{cut}$, where r_{cut} is the distance at which the potential is truncated, and $U_{LJ}(r)$ is the conventional Lennard-Jones (LJ) potential, *i.e.*, $U_{LJ}(r) = -4\varepsilon[(\sigma/r)^{12} - (\sigma/r)^6]$. The parameter ε corresponds to the energy scale of the interaction and σ is related to the characteristic diameter of the beads d, *i.e.*, $\sigma = d/2^{1/6}$ and $d = 50$ μm. The choice of the r_{cut} value determines the nature of the potential $U^{cut}_{LJ}(r)$: *repulsive*, which is also known as Weeks–Chandler–Andersen (WCA) potential for truncated Lennard-Jones potential in minimum $r_{cut} = 2^{1/6}\sigma$, and *attractive* for a commonly chosen $r_{cut} = 2.5\sigma$. The presence of attractive interactions between particles is reminiscent of a Stockmayer fluid, a simple and convenient model for representing ferrofluids[50,51] or lattice of particles stabilized by dipolar coupling.[52]

The colloidal structures analyzed here are modeled to represent the colloidal magnetic particles that have iron oxide inclusions inside the silica shell: *attractive* part of isotropic interaction; we choose a weak interaction between particles,[52] $\varepsilon_a = 3.5 \times 10^{-19}$ J ($\varepsilon_a = 0.3U_{\uparrow\uparrow}$ for $d_{core} = 10$ μm) and $r_{cut} = 125$ μm for particles with diameter $d = 50$ μm. The value of the sphere repulsive contact potential is taken as $\varepsilon_r = 7 \times 10^{-16}$ J for particles with the same diameter $d = 50$ μm (*i.e.*, $\varepsilon_r = 10U_{\uparrow\uparrow}$). The magnitude of the attractive part of potential and interaction range can be varied by controlling the colloidal charge number or surface composition.[53]

We study the system by means of Langevin molecular dynamics computer simulations (described in the following subsection): our spheres are represented by WCA potential, and carry a magnetic point dipole in their centers. A weak isotropic van der Waals (vdW) attraction between the spheres is included for a more realist approach to an experimental solution of colloidal particles. In the experiment, the colloidal particles are stabilized against irreversible agglomeration by vdW forces, either by polymers grafted to the surface, or manipulating the ionic content of the fluid. The vdW attraction between the spheres provides additional stability to the lattice composed of assembled tubes after the electromagnetic field has been switched-off. As such, our results can be scaled to different shell materials, *i.e.*, polystyrene and silica oxide, but the conclusions of this minimal model should be generic.

2.3. Interaction with conductive wire

We place the conductive wire in a suspension of spherical magnetic particles. The conductive wire is an elegant way to cover the cylindrical surface with magnetic particles. Such a system has been recently implemented by Bécu *et al.* with paramagnetic particles.[44] When replacing paramagnetic particles with magnetic particles, the magnetic fields of the ferromagnetic particles and the electromagnetic field generated by the conductive wire become independent. As a result, we obtain an additional tuning parameter – a ratio between magnetization of the particle and electromagnetic field or current of the wire. Still, the system parameters should be carefully selected to avoid the formation of kinetically trapped clusters or arcs of particles attached to the wire.

We consider a situation in which colloidal suspension is placed in the vicinity of the current conducting wire. A wire with outer diameter $2R_w = 50$–100 μm is connected along the z-direction. In order to generate an electromagnetic field able to attract particles at the surface of the wire, significant cur-

rents must go through the wire, giving rise to fields of several mT at the wire surface. Recent similar experiments with paramagnetic particles indicate that a 50 μm wire can support currents of up to 0.5 A for several minutes and up to 0.8 A for a short time, creating electromagnetic fields up to B = 3.2 mT,[44] *i.e.*, $B_w = \mu I/\pi(2R_w + d)$ for d_w = 50 μm wire and d = 50 μm particle.§ We will show how the interactions between the particles and of particles with the wire can be balanced to obtain single wall tubes. Our design based on ferromagnetic particles has a freedom of tuning the ratio between two magnetic forces: interparticle magnetic force F_{mm} and electromagnetic force between ferromagnetic particles and the conductive wire F_{mI}, *i.e.*, magnitude of magnetic force between two particles depends on the square of their magnetic moments and the force between particles and conducting wire depends linearly on the magnetic moment. At the same time, magnetic moment is proportional to the cube of the core's diameter allowing the variation of the ratio for up to three orders of magnitude, therefore this ratio can be anywhere between F_{mI}/F_{mm} = 1–1000 (the single wall tubes will be created only at the higher ratios).

2.4. Langevin molecular dynamics

Langevin molecular dynamics (MD)[54] was used to study the self-assembly in the vicinity of the wire under the influence of an electromagnetic field of uninsulated conductive wire. The total force of implicit solvent on each particle has the form: $\vec{f} = \vec{f}_c + \vec{f}_f + \vec{f}_r$, where f_c is the conservative force of interparticle interactions and of particles with the wire, $f_f = -(m/\xi)v$ is a frictional drag or viscous damping term proportional to the particle's velocity, and $\langle f_r \rangle = \sqrt{k_B T m/\xi}$ is the random Brownian force of the solvent. The random force term is treated as a Gaussian process that adheres to the fluctuation–dissipation theorem. The rotational degrees of freedom are, of course, governed by the equations of motion for the torque and angular velocity of a sphere. Since evolution in time is not of primary concern in this study, the values of mass, inertia and translational/rotation friction coefficients are physically inconsequential to the final state of the system. An estimate of time, per MD step, can be obtained for 50 μm-sized colloidal particles with d_{core} = 20 μm as $t = \sqrt{M_{sp} d^2/U_{\uparrow\uparrow}} = 80$ ms (mass of the core–shell hematite/silica particle M = 10 μg). The total length of the MD simulation was thus estimated to be of the order of 15 minutes (*i.e.*, about 1000 s).

2.5. Energy minimization

The energies of finite tubes were independently computed using 10–10^3 initial configurations with random magnetization (depending on the size of the system). The procedure included two steps: in the first step 'overdamped' equations of rotational motion of each particle were integrated with respect to the torque excreted on a particle (same equation as in Langevin molecular dynamics equations as in the previous section). The parameters used correspond to motion in a highly viscous fluid where angular velocity is proportional to torque, *i.e.*, in the limit where no acceleration takes place, in order to avoid any oscillations. In the second step, the resulting configurations were used as the input to a rigorous conjugate gradient minimization algorithm.[55] The second step was required since 'overdamped' rotational motion converges slowly towards the ground state¶ for a prescribed geometry. The energies of the resulting configurations were compared – about 10% of configurations had the same energy, in the limit of numerical precision of about $\delta u/u = 10^{-7}$, corresponding to the ground state. The minimization procedure always finds dipole moments tangential to the cylindrical surface, *cf.* ref. 20.

2.6. Geometry of tubes

We refer to tubes made by stacking of rings.‖ In AA-tubes all constitutive rings are exactly aligned, *cf.* Fig. 1(a), and in AB-tubes every ring is shifted by half of the particle's diameter, in respect to its preceding ring, *cf.* Fig. 1(b). Alternatively, AA- or AB-tubes could be generated by rolling square or triangular lattices with cylindrical confinement, respectively.

Particle i-positions in AA tubes are calculated as: $x_i = R\cos(2\pi i/N)$, $y_i = R\sin(2\pi i/N)$, and $z_i = \lfloor i/N \rfloor d$, where $\lfloor x \rfloor$ is the greatest integer function and gives the largest integer less than or equal to x, while N is the number of particles in a constitutive ring. To simplify the discussion, we refer to N also as *curvature* since there is a correspondence with the tube's geometrical curvature $R/d = 1/2\sin(\pi/N)$, *e.g.*, we obtain $R/d = \sqrt{2}/(\sqrt{3}-1) \approx 1.3$ for N = 8 ring.

One of the ways to obtain AB tubes is stacking of a pair of two successive rings.** In both rings particle positions are calculated based on their index i: $x_i = R\cos(2\pi i/N + \theta_i)$, $y_i = R\sin(2\pi i/N + \theta_i)$, and $z_i = \lfloor i/N \rfloor \Delta z$, where θ_i is the angular displacement of rings $\theta_i = \pi \mathrm{mod}(\lfloor i/N \rfloor, 2)/N$ and

§ To favor the comparison with previous research on paramagnetic particles, we present here results for wires with $2R_w$ = 100 and 130 μm and particles with 50 μm diameter. Ohmic heating limits the current through wire and is proportional to the square of the current and wire radius. Since the electromagnetic field B is linearly proportional to the current and inversely proportional to the distance of centers of the particle and wire, the power is $P \propto B^2(1 + d\backslash R_w)^2$. Therefore, we should note that the increase of the wire diameter allows higher electromagnetic field for similar dissipation.

¶ A simple example of a discrete ground state is two dipole cases: put two dipoles next to each other and let them orient freely in three dimensional space, they will align their moments in a head to tail configuration (coaxially).

‖ Apart from self assembly on the micro-scale, it is possible to construct tubes described in this subsection manually on the macroscopic (millimetre) scale. The neodymium magnetic spheres are widely available and applicable for building model systems.[56] Neodymium magnets are made of a sintered alloy of iron, neodymium, and boron ($Nd_2Fe_{14}B$). The coercive field strength is about 10^6 A m^{-1}. Thus, the neodymium magnets can withstand high external magnetic fields. The remanence of 1 to 1.5T is at the same time not larger than that in other magnetic materials. All tubes constructed in this section can be therefore built with neodymium magnets.

** The tubes can also be created, in analogy to carbon nanotubes, by rolling a ribbon of a triangular lattice on a cylinder surface.[20] The cylindrical geometry is infinite in one direction and we can, in analogy with crystal lattices, generate tubes by periodical reproduction of a curved patch (unit cell) along the helical backbone with *spanning vectors* $(\vec{a}_1, \vec{a}_2)$. This curved unit cell has n_1 particles along the $\vec{a}_1$ direction and n_2 particles in the $\vec{a}_2$ direction.

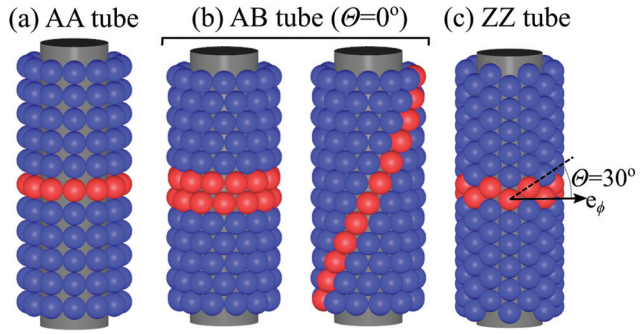

Fig. 1 Illustration of (a) AA, (b) AB, and (c) ZZ tubes. The tubes are wrapped around the confinement cylinder. Tubes can be created *via* ring stacking (highlighted). A single ring is enough in the case of AA and ZZ tubes. We show that AB tubes can be created in two ways. The first way is by a pair of successive rings in the case of the AB tube (left panel, see ESI movie 1†). The second way is by wrapping of the ribbon with a triangular lattice on cylindrical confinement (right panel, see ESI movie 2†). In the right panel of the AB tube, the edge of the ribbon with 12 threads is denoted. The ZZ tube can be created in three ways, stacking of zig-zag rings (pictured), wrapping 14 filaments parallel to the tube's long axis, or 14 thread ribbons oblique to the axis (see ESI movies 3 and 4†). The AB tube has a chiral angle $\Theta = 0°$. The lattice structure of the ZZ tube is triangular, like one of the AB tubes, while chirality is different, *i.e.*, $\Theta = 30°$.

$\Delta z = \sqrt{d^2 - 2R^2[1-\cos(\pi/N)]}$ is the displacement between successive rings along AB tube's axis and $i = 1, N_{\text{tube}}$. The total number of particles in the tube N_{tube} is a multiple of the number of particles in ring N and the number of rings N_{rings}, *i.e.*, $N_{\text{tube}} = N_{\text{rings}}$.

In addition to stacking of the rings, the tubes can be created by rolling a ribbon with a square or triangular lattice on a cylindrical surface. The right side panel in Fig. 1(b) shows an edge of the ribbon creating exactly the same structure as that by stacking of rings (see also ESI movies 1–4†). In fact, every ordered tubular structure can be generated by reproduction of a curved unit cell along the helical lines defined through curved spanning vectors in analogy to crystals in two dimensions. This curved unit cell has n_1 and n_2 particles along two spanning directions.[20]

Still, there are geometrical limits for a ribbon with a defined structure (*i.e.*, square, rhombic or triangular). Like in carbon nanotubes, ribbons of assembled particles can be rolled at specific and discrete ("chiral") angles. The chiral angle can take values $0 < \Theta < 30°$ for triangular lattices and $0 < \Theta < 45°$ for square lattices, where Θ is the angle between the thread of particles and tangent to the cylinder radius[57] (in Fig. 1). Here, we will demonstrate how combination of the rolling angle and radius decides the tube's properties with respect to magnetic state energies. We show AB and ZZ tubes which have different chiralities, $\Theta = 0°$ and 30°, in Fig. 1(b) and (c), respectively. The circular arrangement of the AB tube corresponds to, the so called, armchair carbon nanotube equivalent. The curvature of the two structures is also similar $R_{\text{AB}}/d = 1.932$ and $R_{\text{ZZ}}/d = 1.945$, while the number of particles in a constitutive ring is different, $N = 12$ and 14 for AB and ZZ tubes, respectively. An arrangement, circular or helical in the AB tube and axial or helical in the ZZ tube, corresponds to a possible choice of magnetization of tubes that is aligned with their lattice structure.

3. Ampère force driven assembly

The central mechanism driving the adhesion of particles on a conductive wire is an interplay between dipolar forces between particles and radial attractive Ampère force. The electromagnetic field of the conducting wire is strong enough to determine the orientation of all dipole moments. In order to obtain a single layer of magnetic particles, the Ampère force should dominate inter-particle dipolar forces. Here, we should point out that the Ampère force generated by the current in the wire depends linearly on the magnetic moment of the particles while magnetic dipolar interactions scale quadratically. Besides, there are symmetric and short-range forces between colloidal particles due to their surface design. We base our analysis on a simplest analytically tractable model for constitutive ring rearrangement and comparison with the MD simulations.

In the following two sections, we first give analytical results for Ampère force driven processes. After that, we compare these analytical results with the ones obtained by computer simulation for moderate and strong currents. We will show that only sufficiently strong current is able to pull and attach all particles to the wire's surface.

3.1. From self-assembled chain to ring

The first agglomeration phenomenon analyzed analytically is the strength of the curved electromagnetic field needed to reduce the radius of an arc built by magnetic particles. An elongated chain (or cluster of chains) should overcome the elastic barrier preventing its bending into the ring under the influence of a circular electromagnetic field. The origin of the resistance to deformation can be understood in terms of a transition from local (chain) to global energy minima, corresponding to a ring or stacking of the rings.[26,58] For simplicity, we assume that the magnetic spheres have a magnetization that follows the curvature of the arc (*i.e.*, part of the ring) and that the arc backbone follows electromagnetic field streamlines (*i.e.*, co-centered with wire).

To do so, we consider a thin wire ($r_{\text{dist}}/R_{\text{wire}} > 1$). An arc with curvature d/R can be obtained by calculating the particle positions based on their index i in Euclidian space: $x_i = r_{\text{dist}}\cos(\theta_i)$, $y_i = r_{\text{dist}}\sin(\theta_i)$, and respective magnetization $m_i^x = \cos(\theta_i + \pi/2)$, $m_i^y = \sin(\theta_i + \pi/2)$, where θ is the angular displacement of particles $\theta = 2\arcsin(d/2r_{\text{dist}})$ and d the particle diameter. The combined resistive magnetoelastic force tries to straighten the chain and reduce its curvature d/r_{dist}, see dashed lines for $N =$ 4,6,12 particles in Fig. 2(a). Due to the circular nature of the electromagnetic field, the curvature d/r_{dist} of the arc is inverse of its distance from the wire r_{dist}. The magneto-elastic force F

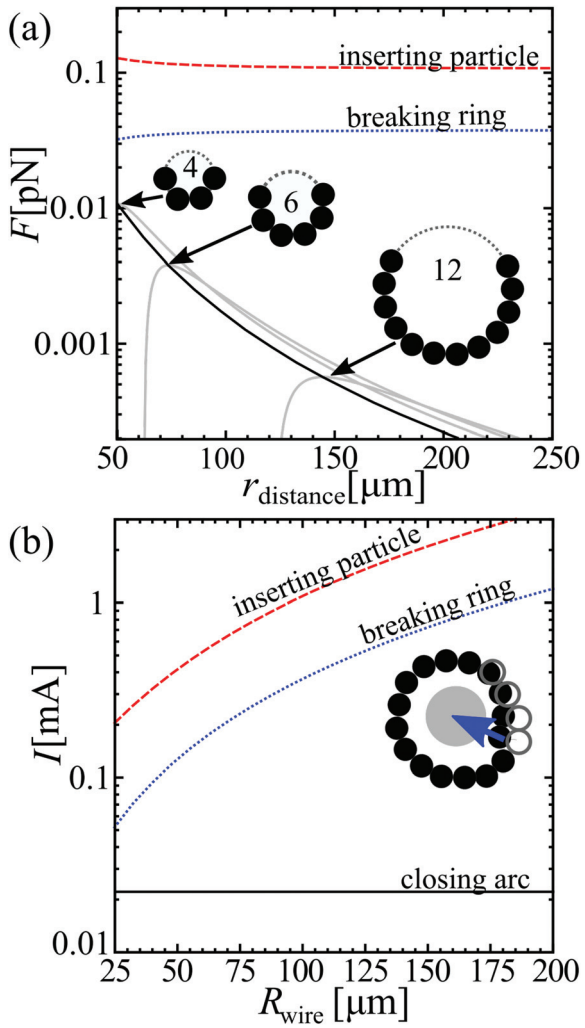

Fig. 2 Critical (a) force and (b) current required to bend and close an arc of particles and form a ring, break the ring, or insert particle between the two rings. The dependence of the forces on distance from the center of the wire r_{dist} is shown. The ring is broken when Ampère's force pushes one side of the ring inside (spirally deforming ring). The evolution of the force with the distance from wire $r_{distance}$ is also shown in figure (a) with dotted line for N = 4,6, and 12 particles. The critical current depends on wire radius R_{wire} since particles become further away from the center. The magnetic moment of the particle is 1.15 A μm^2.

increases up to the point when the arc ends start to attract each other, *cf.*, bold black line connecting maxima of force curves for different arcs in Fig. 2(a). The critical force for the chain with N = 4 particles has a maximum F = 30 pN at distance r_{dist} = 50 μm and N = 6 particles has F = 15 pN at r_{dist} = 70 μm. Thereafter, the deformation of the chain becomes irreversible. The magneto-elastic force decreases with increasing curvature d/r_{dist} and changes the sign. The negative force means that after that point the arc closes on its own. Also, one can observe that while the critical force diminishes with distance – the highest necessary critical current is for thin wire and short arcs (*i.e.* for three particle arc). The critical force is inversely proportional to the distance, *i.e.*, $F \sim 1/r_{dist}$. The current needed to generate sufficient electromagnetic field, $I \approx 0.02$ A, is therefore independent of the chain length.

3.2. Attaching particles to the surface of the wire

We also observe that for a moderate current the long arc closes into a ring with a radius larger than the radius of the wire (R_{wire}). How does this ring finally attach to the surface of the wire? What is the critical force and current required to break the rings by spiral deformation? The transformation from a large ring to the adapted wire diameter involves a destabilizing field able to tear apart a ring by pulling a part of it inwards to the surface of the wire ($r_{dist} > R_{wire}$). The energy per particle of the single ring is:

$$u_r(N) = -\frac{1}{4}\sin^3\left(\frac{\pi}{N}\right)\sum_{k=1}^{N-1}\frac{\cos\left(\frac{2\pi k}{N}\right)+3}{\sin^3\left(\frac{\pi k}{N}\right)}. \quad (4)$$

Similarly, the approximate expression for the force required to break the ring is given by (see also Fig. 2(a)),

$$F_s(N) = -\frac{3}{8}\sin^3\left(\frac{\pi}{N}\right)\sum_{k=1}^{N-1}k\frac{\cos\left(\frac{2\pi k}{N}\right)+3}{\sin^3\left(\frac{\pi k}{N}\right)}. \quad (5)$$

Since the Ampère force reaches its strongest value in the wire surface, the ring will break in the vicinity at this position. We can therefore estimate the critical current to be $I = 2\pi(d + R_{wire})^2F/\mu_0 m$, as shown in Fig. 2(b). The current required to break a ring is more than three times higher than the current needed to close an arc and increases with the wire radius. Still, the increase is slow ($I \sim R_{wire}^{\alpha}$, where $\alpha < 1$) and is compensated without the increase in current density through the wire.

The magnetic particles stick (or diffuse) on top of the triangular lattice formed on the cylindrical surfaces. Following compaction, the remaining beads coming from solvent try to pop-in between the constitutive rings of the tube. In numerical analysis, we use the fact that a ring configuration compensates for the dipole moment and the total dipole moment is zero within the ring. In far field, the electromagnetic field of the ring resembles a multipole, *i.e.*, the electromagnetic field drops with the distance as $1/r^{N+2}$, where N is the number of particles in the ring. The self-screening of inter-ring dipolar interactions takes place as soon as the rings are separated by more than one particle size. Therefore, the change in total energy depends dominantly on the distance of the touching rings, *i.e.*, the change in their interaction energy,

$$u_{ir}(N) = -\frac{1}{8}\sin^3\left(\frac{\pi}{N}\right) \times \sum_{k=0}^{N-1}\frac{2\left\{3+\cos\left[\frac{\pi(2k+1)}{N}\right]\right\}\sin^2\left[\frac{\pi(2k+1)}{2N}\right]+dz^2S_k}{\left\{dz^2\sin^2\left[\frac{\pi(2k+1)}{2N}\right]+\sin^2\left(\frac{\pi}{N}\right)\right\}^{5/2}} \quad (6)$$

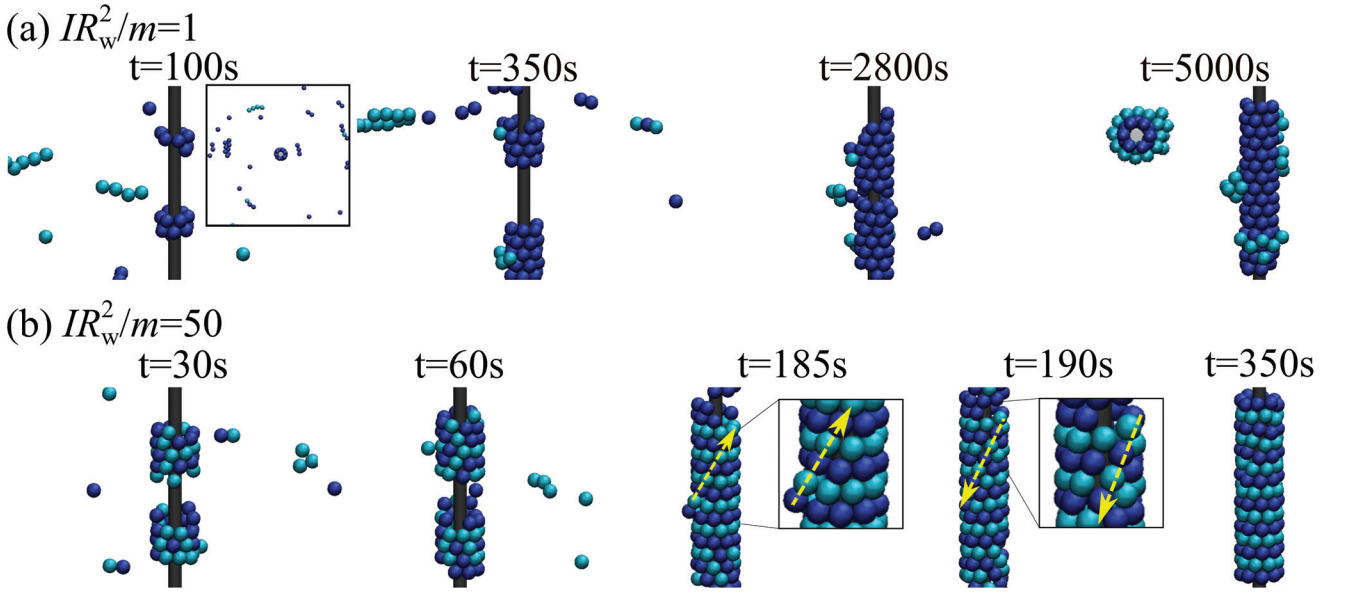

Fig. 3 Snapshots of MD simulations at moderate (a) IR_w^2/m = 1 and strong (b) IR_w^2/m = 50 currents are shown. (a) For IR_w^2/m = 1, we observe chains form as an oriented collection of magnetic dipoles, increasingly curved by the electromagnetic field as they approach, and eventually attach to the wire. The particles in contact with wire at t = 1000 s are colored differently. The animation is given as ESI movies 5 and 6† (top and side views). (b) At strong currents, IR_w^2/m = 50, Ampère force inserts particles into the triangular lattice. Insets between t = 53 s and 54 s show particles while entering moving (shear) tube's structure turning it into a quasi-stable single stranded helix. The particles belonging to successive rings are colored differently at t = 185 s to visualize this process. After some time, t = 190 s, the helix shears back into a tube with rings of magnetic particles conforming electromagnetic field lines. The animation is given as ESI movie 7.† The magnetic moment of the particle is 1.15 A μm^2, the wire radius is (a) $R_w = d$ = 50 μm and (b) $R_w = 1.3d$ = 65 μm, and the current is (a) I = 0.46 mA and (b) I = 23 mA.

where dz is the distance between touching rings and $S_k = \sum_{i=0,1,2} (-1)^i \binom{2}{i} \cos[\pi(2(k+i)-1)/N]$. We estimate the force $F_i(N) = (6/\sqrt{2})\partial u_{ir}(N)/\partial dz$ needed to push the particle between the two rings in contact, *i.e.*, at a distance:

$$dz_N^c = \sqrt{1 - \frac{1}{2}\left[1 - \cos\left(\frac{\pi}{N}\right)\right] \sin^{-2}\left(\frac{\pi}{N}\right)}. \quad (7)$$

The resulting critical force and current depend on the wire radius as shown in Fig. 2(a) and (b), respectively. For wire of R_{wire} = 65 μm, on which 8 particles of d = 50 μm could form a ring, the critical current is I = 0.4 A.

3.3. Dynamics of assembly

We simulate the Ampère force driven assembly of colloidal magnetic particles on a cylindrical confinement. The snapshots of evolution of the configuration with time are given in Fig. 3 and animations are given in the ESI as movies 5–7.† We model the dynamics of assembled particles with dipolar coupling in the presence of the circular electromagnetic field generated by the electrical current going through a conductive cylindrical wire which, at the same time, serves as a geometrical constraint.

In MD simulations at moderate currents, *cf.* the inset in Fig. 3(a), we observe the formation of chains composed of an oriented collection of magnetic dipoles, increasingly curved by the electromagnetic field as they approach, and eventually attach to the wire. This process is schematically given in Fig. 2(a). The resistance to bending increases as the particles approach the wire. The chain finally bends due to the fact that the dipoles cannot align with both, the electromagnetic field lines and with each other's magnetic axis. In this frustrated configuration, the magnetic field of each dipole exerts a torque on all other dipoles.

At sufficiently high currents we observe that the system becomes rapidly compact, see Fig. 3(b). We also observe, between t = 185 s and t = 190 s in Fig. 3(b),†† how the last particle coming from solvent pushes the already formed triangular lattice structure forming a metastable single stranded helix. In this metastable state, the helix backbone and electromagnetic field are not aligned, resulting in mechanical strain on the whole structure. At t = 350 s, we observe that the system shears back into a stable state (tube) with constitutive rings aligned with the electromagnetic field.

Finally, we should note that a square lattice can only be obtained by self assembly on a square patterned surface. This corresponds also to the state-of-the-art in the literature.[41] The latter one is limited to the self assembly of finite sized structures. Nano-scale printing allows realization of curved conductors with a complex surface geometry and opens an interesting playground for generating different packings of magnetic spheres. The Joule heating limits the current through a

†† The particles are colored differently to visualize the movement.

100 μm wire to 0.5 A.[44] Therefore, the magnetic moment of the particle is limited by the total magnetic moment of the particle and should be $m < IR_w^2/50 = 25$ A μm^2, taking into account the whole size of the particle. The total magnetic moment of the particle is controlled by the volume of the ferromagnetic core and choice of the magnetic material. Once the dipolar tube had been formed, the particles would stay in place after the wire is removed. The tubular structures are mechanically stable also at finite temperatures (see movie 8 in the ESI†). We should highlight that the wire is not only a confinement structure but an efficient way to control the magnetic configuration of these tubes.

4. Magnetization of dipolar tubes

In this section, we analyze the implication of curvature and size effects on the energy landscape of triangular and square lattices. The isotropic interaction between the particles and the particles with the wire, which now serves only as a rigid cylindrical confinement, does not have influence on magnetic dipole orientation.

4.1. Characteristics of triangular and square lattices

First, we investigate the dependence of ground state energy on magnetization. All dipoles in the triangular lattice are parallel and allowed to rotate only around a fixed axis orthogonal to the plane, see Fig. 4(a), for numerical details *cf.* ref. 59. There is a continuous ground state for any in-plane angle θ with cohesive energy value $u_{AB} \simeq -2.7586$,‡‡ see also ref. 7 and 8. For a square two dimensional lattice, similarly, there is a continuous degeneracy of its ground state, described in Fig. 4(b) and (c). A continuous state, in this case, involves a unit cell of four particles. The moments in a unit cell are synchronously coupled and in our notation take directions θ, $\pi - \theta$, $\pi + \theta$, and $-\theta$, in the anti-clockwise direction as shown in Fig. 4(b). The ground states found are obviously antiferromagnetic, with the total dipole moment within the cell conserved and equal to zero. The most striking is the so-called *vortex state* for $\theta = \pi/4$ with a fully enclosed circulation of the magnetic dipole moment within the unit cell. The ground state cohesive energy value is $u_{AA} \simeq -2.5494$.§§ We will use the calculated ground state energy value as an absolute point for comparison of energies of different states in tubes with square or triangular lattice structures. We should note that both antiferromagnetic states are observed in systems of square particles as a result of the interplay between the magnetization defined by crystallinity of the cubes and the structure of the two dimensional super lattice.

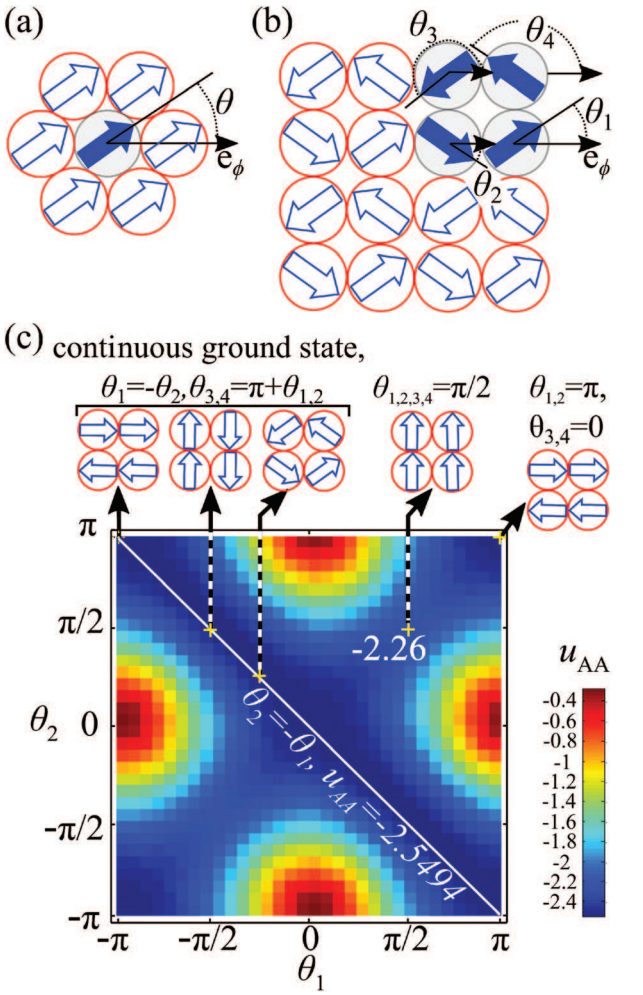

Fig. 4 Visualization of degenerate states in infinite (a) triangular and (b) square lattices, *i.e.*, respectively AB and AA packings. The dipoles are depicted as arrows located in the center of the spheres. In the case of the triangular lattice the unit cell consists of a single particle and in the case of the square lattice it consists of four particles (gray). (c) An energy landscape for the square lattice is shown with respect to two θ_1 and θ_2 out of four magnetic moments in the unit cell. Other two moments were oriented so the energy of the system is minimal. One can observe a flat valley of degenerate ground state, $\theta_2 = -\theta_1$, with energy $u_{AA} \simeq -2.5494$. The saddle point which represents a uniformly magnetized square plane with energy $u_{AA}^{sdd} = -2.26$ is also marked. The curves are drawn through the discrete points and are smooth. The results are in principle scale independent. The reference magnetic energies are $U_{\uparrow\uparrow} = 10^{-18}$ J and 67×10^{-18} J, *i.e.*, $256k_BT$ and $1.6 \times 10^4 k_BT$, for particles with magnetic moments $m = 1.15$ A μm^2 and 9.2A μm^2, respectively, where $T = 300$ K is the temperature and k_B is the Boltzmann's constant.

Commonly, magnetic cubes are represented by single dipoles placed in the center. While this is a good approximation for many systems, it only takes into account about 50% of the total volume of the cube and is neglecting the effect of the corners. Therefore one could expect degeneracy breakup due to asymmetry of the shape of the cubes. Still, the cubes are synthesized very often with curved edges, *i.e.*, as superballs, exhibiting a continuous transformation of shape from an ideal cube to a sphere[60] and they are expected to self assemble in structures

‡‡The energy of the continuous ground state of the triangular lattice independent of the in-plane angle θ is $u_{AB} = -2\zeta(3) + 16\pi^2 \sum_{k=1}^{\infty}\sum_{l=1}^{\infty} \cos(kl\pi) K_0(kl\sqrt{3}\pi) \simeq -2.7586$.

§§The energy of the continuous ground state of the square lattice is $u_{AA} = -2\zeta(3) + 16\pi^2 \sum_{k=1}^{\infty}\sum_{l=0}^{\infty} k^2 \{K_0[4k(l+1)\pi] - K_0[2k(2l+1)\pi]\} \simeq -2.5494$.

with a square symmetry.[61] An extent of degeneracy breakup remains to be analyzed during this shape-shift.

4.2. Degeneracy break-up with curvature

Wrapping of the plane around the confinement cylinder will make the system quasi one-dimensional and break degeneracy. We will discuss repercussions of degeneracy breakup on cohesive energy for different dipole orientations. We analyze first the degeneracy breakup in infinite tubes: according to tube's cylindrical geometry, we represent the dipole moment of the i-th particle in cylindrical coordinates like:

$$\vec{m}_i = m_{i\phi}\vec{e}_\phi + m_{iz}\vec{e}_z, \tag{8}$$

with constraints $m^2 = m_{i\phi}{}^2 + m_{iz}{}^2$ (i = 1,...N). The parallel component with respect to tube's axis is given by m_z and the orthogonal component is m_ϕ (*i.e.*, m_ϕ is tangential to cylinder's circumstance). In Fig. 5, we follow the dependence of energy on angular parameter θ, $m_{iz} = m\sin(\theta)$. We find that the axial magnetization (*i.e.*, $\theta = \pi/2$) of dipole moments represents the ground state for both AA- and AB-tubes, and circular magnetization (*i.e.*, $\theta = 0$) is the most unfavorable as seen in Fig. 5.

Between circular and axial magnetization (*i.e.*, $0 < \theta < \pi/2$), we observe a continuous increase of energy with increasing circular alignment of magnetization. These transition states, we call *vortex* in the case of square AA tubes and *helical* in the case of triangular AB tubes, *e.g.*, $\theta = \pi/4$ in Fig. 5(a) and (b), respectively. The cohesive energy, of different configurations shown in Fig. 5, converges to a continuously degenerate state with increasing curvature N, following the power law, $u^N - u^\infty \sim N^{-2}$, *cf.* the inset in Fig. 5.

Configurations (A1), (B1), (C1), (D1), and (E1) are shown in Fig. 7. The results are in principle scale independent. In this work, we have used in all examples length scale d = 50 μm.

4.3. Magnetization states in finite tubes

We will go one step further and consider finite tubes which consist of N_{rings} stacked rings. Tube's length influences ground state dipole orientation on both global and local levels. The competition between the two geometrical parameters, (i) curvature N and (ii) tube length N_{rings}, leads to different possible magnetic states of the tube. The energies of ground states, at a prescribed number of rings N_{rings} and for two curvatures N = 8, 12, are given in Fig. 6 for AA and AB tubes (*i.e.* square and triangular tubular structures).

Points (A2), (B2), (C2), (D2) and (E2) from the state diagram are chosen as illustrative examples in Fig. 9. The results are in principle scale independent. We used length scale d = 50 μm.

Finite AA tubes. For square AA stacked tubes with N = 12 curvature, the circular magnetization state is stable for (2 ≤

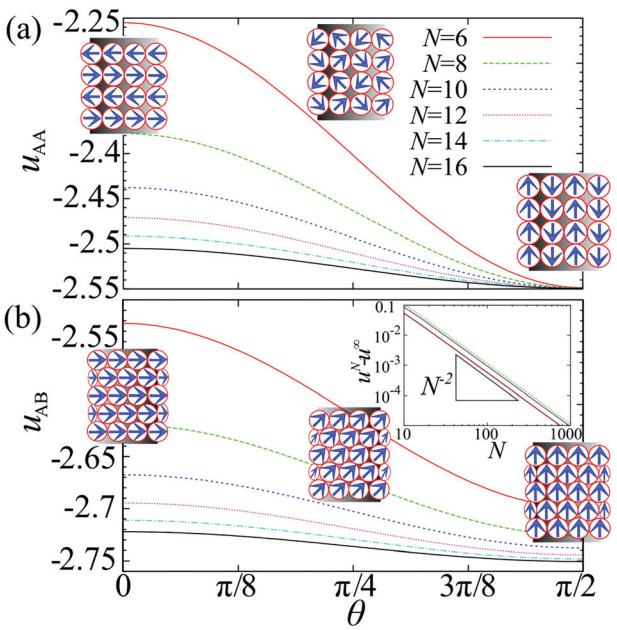

Fig. 5 Dipolar cohesive energy spectrum of configurations for dipole orientations shown in Fig. 4 on a curved surface of the infinitely long tube with (a) square AA and (b) triangular AB tubes. Breaking of degeneracy with respect to angle θ due to the curvature, *i.e.*, proportional to the number of particles in the constitutive ring N, is shown. The axial magnetization corresponds to $\theta = \pi/2$. The inset shows convergence of dipolar cohesive energies for $\theta = 0$, and $\pi/4$ to infinite two dimensional plane value u (for square lattice $u_{AA} = -2.5494$ and for triangular lattice $u_{AB} = -2.7586$). The reference magnetic energies are $U_{\uparrow\uparrow} = 10^{-18}$ J and 67×10^{-18} J, *i.e.*, $256k_BT$ and $1.6 \times 10^4 k_BT$, for particles with magnetic moments m = 1.15 A μm^2 and 9.2A μm^2, respectively, where T = 300 K is the temperature and k_B is Boltzmann's constant.

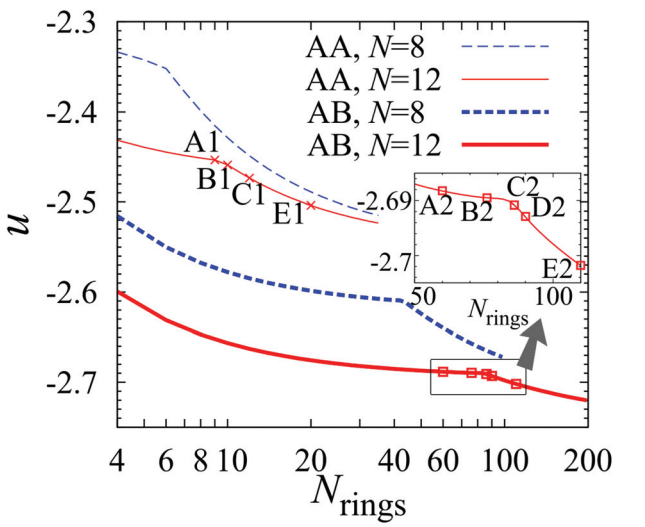

Fig. 6 Reduced cohesive energy profiles u as a function of the number of rings N_{rings} for AA and AB tubes with curvatures N = 8 and 12. Configurations for points (A1), (B1), (C1), and (E1) are shown in Fig. 7 and (A2), (B2), (C2), (D2) and (E2) in Fig. 9. The curves are plotted through the discrete points and serve as guide to the eye, all points lie on the curves, and only a few listed and analysed points are shown. Before points (A1) and (B2) the magnetization is ideally circular and the energy decrease is only driven by the addition of new rings. The results are in principle scale independent. Two possible choices for reference magnetic energy could be $U_{\uparrow\uparrow} = 10^{-18}$ J and 67×10^{-18} J, *i.e.*, $256k_BT$ and $1.6 \times 10^4 k_BT$, for particles with magnetic moments m = 1.15 A μm^2 and 9.2A μm^2, respectively, where T = 300 K is the temperature and k_B is Boltzmann's constant.

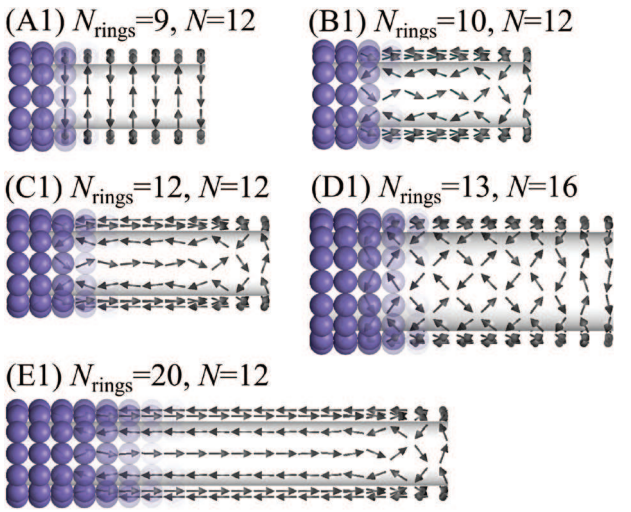

Fig. 7 Illustrative examples of characteristic ground state magnetization for tubes with AA stacking. Configurations (A1), (B1), (C1) and (E1) are obtained with curvature N = 12, and (D1) with N = 16.

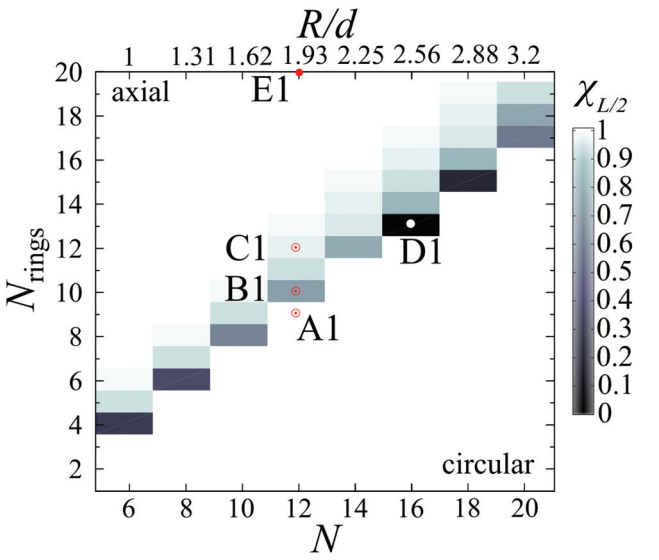

Fig. 8 State diagram of AA tubes. It is shown in 2D tube length-curvature parameter space, *i.e.*, $L(R)$ or $N_{rings}(N)$, with clear indication of axial, circular and transitional vortex magnetization states. The coloring method based on order parameter $\chi_{L/2}$, defined in eqn (9), is applied. The order parameter $\chi_{L/2}$ is zero in axial and circular magnetic states, *i.e.*, when the magnetic texture is parallel to tube geometry, and equal to unity when the magnetic structure is turned by 45° (*i.e.* equidistant from axial and circular magnetization).

$N_{rings} \leq 9$) rings. It turns out that circular magnetization is the ground state of short tubes, relative to their constitutive ring size N. The circular magnetization case N_{rings} = 9 is illustrated in Fig. 7(A1). The change in magnetization towards axial is abrupt for N_{rings} = 10 and curvature N = 12, see Fig. 7(B1). We observe a local antiferromagnetic circulation formed almost over the whole length except in terminal rings. The dipoles in the middle of the tube are only slightly misaligned with tube's axis (*i.e.*, for angle 0.12π). As a result of change in the magnetic order we observe, Fig. 6, that the slope of cohesive energy changes from N_{rings} = 9 to 10, *i.e.*, between points (A1) $u_{AA}^{12,9}$ = −2.4534 and (B1) $u_{AA}^{12,10}$ = −2.4589. Extending further the tube length $N_{rings} \geq 13$, we observe a well formed axial antiferromagnetic state with chains of alternating magnetization parallel to the tube axis.

The state diagram of AA tubes is given in Fig. 8. The calculated equilibrium states are given for different curvatures and lengths of AA. The coloring method in the state diagram is based on the local order parameter, conveniently defined as:

$$\chi_{L/2} = |2\langle (m_z/m)^2 \rangle_{L/2} - 1|, \quad (9)$$

where $(m_z/m)^2$ is the scaled intensity of local magnetization in the axial direction and $\langle\ \rangle_{L/2}$ is the average in the middle of the tube ($z = L/2$).¶¶ The idea of the order parameter is to visualize transition states (between axial and circular). Magnetic states which do not match with axial nor circular states in the middle of the tube are also referred to as *vortex states* in AA tubes. The order parameter measures the misalignment of $\vec{m}$ from the geometry of the tube, it is $\chi_{L/2}$ = 1 in circular, *i.e.*, $(m_z/m)^2$ = 0, and axial states, *i.e.*, $(m_z/m)^2$ = 1, *i.e.*, white areas comprising points (A1) and (E1) in Fig. 8 (*cf.* also Fig. 7). The state diagram contains three regions corresponding to the three classes of equilibrium states. We observe pure circular magnetization with no axial dipole component for short tubes. In the transition state, there is a change from the dominantly axial orientation of dipoles in the middle of the tube ($z = L/2$) to a vortex-like orientation at tube's ends ($z = 0, L$). We observe that a transition from a vortex to an axial state follows roughly a linear trend for $4 \leq N \leq 14$. For N = 16 this trend is broken and the transition occurs earlier (after a single additional ring and not two). The resulting local order parameter is very small, $\chi_{L/2} \approx 0$. This is all a result of a strong local circulation, *i.e.*, $\theta = \pi/4$, $m_\phi = m_z = m/\sqrt{2}$, *cf.* value of $\chi_{L/2}$ at point (D1) in Fig. 8 and also visualization in Fig. 7.

Finite AB tubes. In the case of AB stacked tubes (triangular lattice), for N = 12 curvature, the circular state is stable for ($2 \leq N_{rings} \lesssim 70$) rings. After that, only dipoles in the middle of the tube significantly start to change magnetization, *cf.* Fig. 9(A2) and (B2). Only when the local order parameter, $\chi_{L/2} \approx 0$, we observe a change in the dependence of cohesive energy on tube's length N_{rings}, *cf.* Fig. 9(C2) and Fig. 6 for N_{rings} = 85. The energy for configuration (C2) is $u_{AB}^{12,85}$ = −2.6895. The similarity of observed state transitions with increasing length of the dipolar tube to state transitions observed in solid magnetic nanotubes is striking.[13,18] This is surprising due to the absence of the exchange interaction in dipolar tubes. We call the transition state $\chi_{L/2} \approx 0$ the *helical state*. The helical state, both in solid and dipolar tubes, is a result of the interplay between tube's curvature and length. We find three equivalent

¶¶In the case of even number of rings, *i.e.*, $N_{tot} = 2k$, we take two rings above/below $z = L/2$.

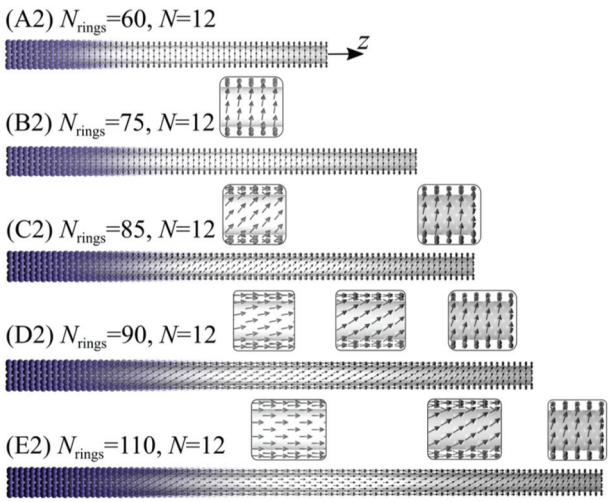

Fig. 9 Illustrative examples of characteristic ground state magnetization for tubes with AB stacking.

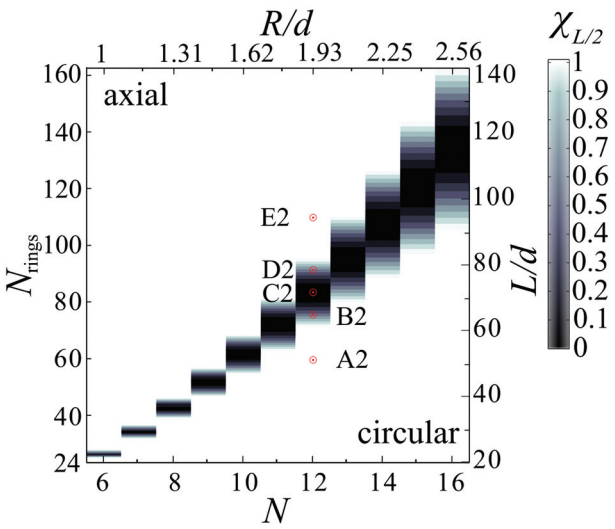

Fig. 10 State diagram of AB tubes. It is shown in 2D tube length-curvature parameter space, *i.e.*, $L(R)$ or $N_{rings}(N)$, with clear indication of axial, circular and transition helical states. The coloring method $\chi_{L/2}$, defined in eqn (9), is applied. The order parameter $\chi_{L/2}$ is zero in axial and circular magnetic states, *i.e.*, when the magnetic texture is parallel to tube geometry, and equal to unity when the magnetic structure is turned by 45° (*i.e.* equidistant from axial and circular magnetization).

states: clockwise, anti-clockwise and symmetric, within numerical accuracy, as a result of broken symmetry.

There are three clear differences between transitions from circular to axial states in AA and AB tubes, as seen in Fig. 8 and 10:

• The transition occurs at smaller tube lengths in the case of AA tubes, *i.e.*, in AA-tubes for curvature $N = 12$ transition is at $N_{rings} \approx 10$ while for AB-tubes it will occur at $N_{rings} \approx 80$;

• For AA tubes, the circular state sharply changes into the transitional vortex state when the threshold length is reached. In the case of AB tubes, the transition through the helical state is gradual with increasing length;

• Edge effects at tube's ends, *i.e.*, in the vicinity of $z = (0,L)$, are much stronger in AB tubes than in the case of AA tubes, *i.e.*, in AB-tubes for curvature $N = 12$ they extend over $\Delta N_{rings} = 30$ rings on each side of the tube, compared to only up to $\Delta N_{rings} = 3$ rings.

It is insightful to compare the energies of obtained finite tubular magnetizations with the limits of an infinite planar triangular and square lattice. In the case of AB tubes for $N = 12$, $N_{rings} = 200$, we obtain $u_{AB}{}^{12,200} = -2.7203$ and an energy deviation of about 15% from the infinite triangular plane case. This is essentially due to the edge effects that are still non-negligible. For much shorter AA tubes, *i.e.*, $N = 12$, $N_{rings} = 35$, we are with $u_{AB}{}^{12,35} = -2.5233$ within 10% from the infinite plane case.

At this point we would like to draw a comparison with solid-state MNTs. In MNTs the magnetic properties are mainly defined by dipole–dipole and exchange interactions, wherein the latter stems from quantum mechanical considerations. Exchange is a short-range interaction that, in micromagnetic approximation, is typically characterized by the exchange length (l_{ex}) that is not larger than a few tens of nanometers. The quantum mechanics signature in magnetic states of nanotubes can be neglected whether by choosing curvature $R \gg l_{ex}$ or reducing the exchange length to zero. The magnetic equilibrium states of MNTs are mostly defined according to the ratio between MNT dimensions, such as their length L and radius R. The radii $R_F \sim \eta l_{ex}$ and $R_V \approx \gamma l_{ex}$ are critical transition radii with $\eta = 1$–10 and $\gamma = 10$–50. In MNTs with $L \geq R$ and $R < R_F$ uniform axial states are the preferred ground states. At $R_F < R < R_V$ and $L \gg R$ the magnetization is in the axial state (*i.e.*, only the center of the tube is axially magnetized), and if the length is reduced to $L \approx R$ magnetization turns into the circular state. The helical state appears as a transition state between the axial and circular states as a result of a reduction of the tube's length. All these states have been predicted theoretically[12,13] and measured experimentally just recently.[14–18] Thus, solid state MNTs with weak or comparable exchange interaction regarding the dipolar interaction will exhibit a circular magnetic order. This is not the case in dipolar tubes, consisting of discrete (nano- or even micro-particles), where exchange interaction is not present. And still, we could find all states seen in MNTs (circular, helical, and axial). We also observe similar tendencies with respect to the tube's size. We find the circular state in short, the helical intermediary state in medium, and the axial state in long dipolar tubes.

The principal difference between the AA- and AB-tubes is the total magnetic moment. For AA-tubes the total magnetic moment is zero. In the case of AB-tubes, the axial and helical states have a finite total magnetic moment, just like MNT counterparts. Fig. 11 shows the dependence of magnetic field intensity on radial distance from the center of AA and AB tubes. The magnetic field at the closest approach of the probe particle $\Delta r/d = 1$ is always smaller than the magnetic field of a single constitutive particle $B/B_0 = 1$ in side by side ↑↓ configur-

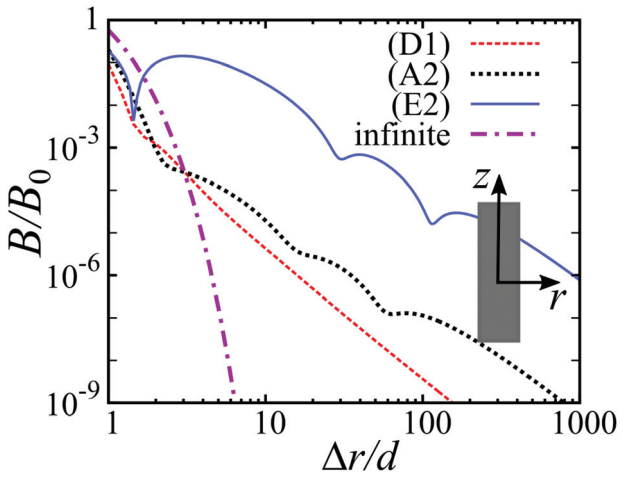

Fig. 11 Dependence of the intensity of the magnetic field B from radial distance $\Delta r = r - R$ from the center of dipolar tubes, where R is the tube radius. The magnetic field is given for the (D1) AA tube in the vortex state $L/d = 13$ long and with curvature $N = 16$, (A2) the circularly magnetized AB tube with $L/d \approx 53$ and $N = 12$, (E2) the axially magnetized AB tube with $L/d \approx 98$ and $N = 12$, and the uniformly axially magnetized infinite AB tube with the same curvature ($N = 12$). The distance $\Delta r/d = 1$ is the distance of the closest approach of the particle to the tube. The configurations of AA and AB tubes are shown in Fig. 7 and 9, respectively. We used length scale $d = 50$ μm. Reference magnetic field is $B_0 = 1$ μT for two particles with magnetic moments 1.15 A μm^2.

ation. The vortex state in the AA tube results in a $B_{D1}(1)/B_0 = 0.09$, while in the case of AB tubes $B_{E2}(1)/B_0 = 0.19$. The smallest structure shown in Fig. 11 has more than 200 constitutive particles, *i.e.*, the (D1) AA tube in the vortex state. In all three cases of the finite tubes, the intensity of magnetic field far from the tube follows the power law on distance, *i.e.*, $B \sim \Delta r^{-3}$ for $\Delta r/L \gg 1$. Only in axially magnetized infinite AB tubes the magnetic field exponentially decays with distance $\Delta r/d$ and therefore fulfills flux closure, *cf.* also ref. 62. This result is not surprising from the micromagnetic point of view since in a finite object a singularity-free solution cannot exist for topological reasons.[63] Only if the system is infinite at least in one dimension, micromagnetic solutions may be constructed. As a result, magnetostatic energy is minimized, leading to similar ground states in finite MNTs and dipolar tubes, that tend to reduce the stray field but cannot make it negligible.

4.4. Chirality and degeneracy breakup

In this section, we would like to point out, how chirality of the structure influences the energy barriers between different states in dipolar tubes. The ribbons of assembled particles can be rolled at different ("chiral") angles Θ. In our self assembly experiment, combination of the magnetic field along the wire and the circular electromagnetic field will result in creating ferromagnetic tubes with a specific chiral angle. We will only briefly analyse limiting cases which are actually the most interesting ones from the point of the metastability (*i.e.*, energy differences between different states). Antiferromagnetic tubes need to be created on a cylindrical structure with a tilted pattern. The radius of these tubes will depend on the lattice structure (*i.e.*, square or triangular) and chiral angle. Here, we will demonstrate how the combination of the rolling angle and radius decides the tube's energy. In the previous section, we have calculated energies of different states for tubes obtained by stacking of the rings. In the following text, we will follow energy gains and losses due to change in the chirality (orientation) of tube's lattice with its axis $\Theta = 30°$ in triangular and $\Theta = 45°$ in square lattices.

First, we will compare the energy of the infinite AB tube shown in Fig. 5(b) and the ZZ tube shown in Fig. 1(c). While the ZZ-tube is aligned with the tube's axis, the ribbon generating AB tube is rolled under a 60° angle, see Fig. 1(b). The energy of the circular state in Fig. 5(b) is $u_{AB}^{circular} = -2.694$ for the unit ring of $N = 12$ particles and $\theta = 0$. The helical state ($\theta = \pi/3$), in Fig. 5(a), is more energetically favorable, $u_{AB}^{helical} = -2.7315$. The axially magnetized state has energy $u_{AB}^{axial} = -2.7441$ for $\theta = \pi/2$. The difference between circular and axial state energies is small, *i.e.*, less than 2% of the total energy. Already at moderate curvatures, *i.e.*, $R/d = 1.932$, the difference in the infinite triangular plane value (u_{AB}^{∞}) is small, $u_{AB}^{axial} - u_{AB}^{\infty} \approx 0.015$ or roughly 0.5% of the total energy value. If we chose chirality to align the tube's structure with its axis, as in ZZ tubes shown in Fig. 1(c),‖‖ the energy converges faster to the infinite triangular plane value. The energy difference, for the system shown in Fig. 1(c), is $u_{ZZ}^{axial} - u_{AB}^{\infty} \approx 0.001$. Improved convergence of the axial state comes with a marginal increase of energy difference to circular and helical states of less than 3% of the total energy value. The energies of circular and helical states, for the ZZ tube in Fig. 1(c), are $u_2^{circular} = -2.618$ and $u_2^{helical} = -2.7$, respectively. We can conclude that by changing chirality we can manipulate energy differences between different states.

The AA tube's square lattice is aligned with the tube's axis, see Fig. 5(a). What will happen if we turn the tube's lattice structure by 45°? We show the configurations and results of energy calculations in Fig. 12. To demonstrate the stability of the structure it is also realized with neodymium magnetic spheres. The striking feature is a comparably small energy increase of $u_{\infty}^{helical} - u_{\infty}^{vortex} = 1.8 \times 10^{-4}$, *cf.* Fig. 12(c). This means that in realization with a finite temperature this system would be degenerate. Since an infinite tube can never be realized, one could ask how significant is the influence of the edges? In this context we calculate energies of finite tubes consisting of $N = 208$ particles, *i.e.*, which correspond exactly to the helical and vortex configurations shown in Fig. 12(A) and (B), and obtain values $u_{208}^{vortex} = -2.4527$ and $u_{208}^{helical} = -2.4495$, respectively. Therefore, at least in these two finite configurations the energy is relatively close to each other (within 2%) and to that of infinite tubes (*i.e.*, within 5%). In contrast to AA tubes in the previous section, the local magnetic order of finite and infinite tubes shown in Fig. 12 is quite similar. The

‖‖ In the ZZ tube, particles form chains (so called, filaments) parallel to the tube's axis.

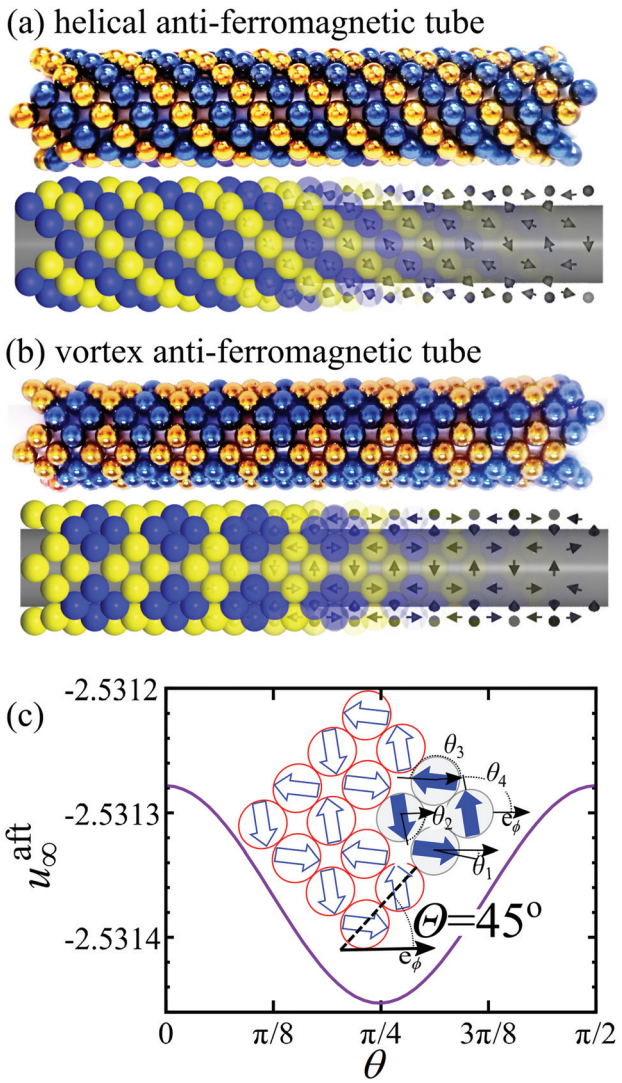

Fig. 12 The helical (a) and vortex (b) anti-ferromagnetic states realized with neodymium magnets (in upper panels) and magnetization pattern. The energy spectrum of configurations (c) for the same infinite configuration with respect to angle θ, where $\theta_1 = \theta$, $\theta_2 = -\theta$, $\theta_3 = \pi + \theta$, and $\theta_4 = \pi - \theta$. The case $\theta = \pi/4$ corresponds to helical and $\theta = 0$, $\pi/2$ vortex state. The chiral angle, *i.e.*, the angle between thread of particles and tangent to cylinder radius, is $\theta = 45°$ and is also marked in the planar scheme of the system in panel (c). To convert results in real units, for example the reference magnetic energies $U_{\uparrow\uparrow} = 10^{-18}$ J or 67×10^{-18} J could be used that correspond to $256k_BT$ or 1.6×10^4 k_BT, in cases of particles with magnetic moments $m = 1.15$ A μm^2 or 9.2A μm^2, respectively, where $T = 300$ K is the temperature and k_B is Boltzmann's constant.

reason is that the tubes finish the crown (zig-zag) ring which prevents formation of a continuous head–tail magnetic order.

5. Conclusion and outlook

In the first part of the paper, we demonstrate that using magnetic particles with a permanent dipolar moment gives additional design freedom for an experiment recently proposed. Injection of an electrical current into a conductor wire induces an electromagnetic field. The radial gradient of this field owns the ability to attract magnetic beads. The particles, therefore, assemble on the wire surface. We explored the intensity of the electromagnetic field that leads to a transformation of the clusters attached to the wire into a single layer tubular structure. We further analyse the limits on the injected currents to minimize the Joule heating and steer the particle assembly. In this regard, we have found a realistic range of currents and resulting electromagnetic fields at which the assembly of spheres and its magnetic orientation are stable and controllable. Our results are generic and can be scaled to many different systems. Once the current is switched off, the circular electromagnetic field disappears, and the particles stay assembled held by interparticle interactions. From this point on, the magnetization of colloidal particles turns and relaxes to the equilibrium configuration.

In the second part of the paper, we studied the curvature-induced breakup of the continuously degenerated state when a two-dimensional ribbon of spheres is curved and transferred to the cylinder. We show that different ferromagnetic states, observed previously,[20,26] are a result of curvature induced energy barriers that lift the continuous degeneracy in the triangular lattice. We performed a systematic investigation of the degeneracy break-up as a function of the tube length and packing symmetry (square or triangular), which lead to a number of equilibrium magnetic states of dipolar tubes. For triangular packing, we show that dipolar tubes transcend the scale. Their equilibrium states mimic the ground magnetization of magnetic nanotubes where the dipolar interaction is either comparable or dominate over the exchange interaction. Indeed, we found the circular state in short tubes, the axial state in long tubes, and the helical state in between. This is an important conclusion since it shows that all these states could exist in magnetic nanotubes also without exchange interactions. We find that the planar square lattice has a continuously degenerate antiferromagnetic state. In tubes with the square lattice, we have found remarkable magnetic vortex configurations formed spontaneously. Such a configuration was observed previously only in a system of magnetic cubes due to intricate relation between the crystallinity of the cubes and packing. Antiferromagnetic states have no analogous in the set of magnetic ground states in continuum magnetic nanotubes[13,21] and are remarkable due to their curvature-induced stability and non-colinear texture. Indeed, these non-colinear states can be very attractive for further research on magnetization dynamics (reversal processes mediated by domain wall propagation and spin-waves) due to the macroscopic scale of dipolar tubes, and therefore less complexity in experiments.

In the context of curvilinear nanomagnetism,[13,25] the present theoretical result could represent a departure point and alternative means to test and explore equilibrium and dynamic magnetic properties at macroscopic scales. The dipolar tubes present an alternative technique to reduce the complexity of experiments and a platform to prove concepts

for applications in magnonics at more accessible parameters (reduced frequencies and macroscopic wavelengths). The experimental realization of cylindrical magnetic objects is very demanding since curvature effects might be overshadowed by wall pinning on imperfections, such as grain boundaries and edges.[21] The realization of presented quasi-one-dimensional or edge free ferromagnets and antiferromagnets would create an accessible platform for testing concepts of spin-based electronics (*e.g.*, Cherenkov-like spin wave emission[22,64] or curvature induced non-reciprocities in magnonics[25,65]) and information technologies by getting around a requirement of robust magnetic uniformity at temperatures of technological relevance. An additional application of the tubular assemblies of dipoles could be modeling of the ordered planar systems due to the absence of the lateral edges in curved geometry and low energy barriers. Macroscopic dipoles were, for instance, successfully used to study frustrated states in spin glasses.[6] Although the previous approach cannot be applied straightforwardly to ordered planar structures, since edge effects could overshadow properties like the response to magnetization reversal, it can motivate further studies on this topic.

Conflicts of interest

There are no conflicts to declare.

Acknowledgements

The authors acknowledge financial support from the European Commission H2020 project DAFNEOX (Grant No. 645658). Numerical calculations were run on the PARADOX supercomputing facility at the Scientific Computing Laboratory of the Institute of Physics Belgrade. I. S. and M. D. acknowledge support of the Ministry of Education, Science, and Technological Development of Republic of Serbia – projects ON171017 and III45018. I. S. and C. G. acknowledge the financial support received by the Proyecto CONICYT PIA/Basal FB 0821 and PCI/atracción de capital humano avanzado del extranjero folio MEC80170122.

References

1 A. P. Ramirez, A. Hayashi, R. Cava, R. Siddharthan and B. Shastry, *Nature*, 1999, **399**, 333–335.
2 M. J. Gingras, *Introduction to frustrated magnetism*, Springer, 2011, pp. 293–329.
3 H. Diep, *Frustrated spin systems*, World Scientific, 2013.
4 J. Loehr, A. Ortiz-Ambriz and P. Tierno, *Phys. Rev. Lett.*, 2016, **117**, 168001.
5 J. W. F. Venderbos, M. Daghofer, J. van den Brink and S. Kumar, *Phys. Rev. Lett.*, 2011, **107**, 076405.
6 P. Mellado, A. Concha and L. Mahadevan, *Phys. Rev. Lett.*, 2012, **109**, 257203.
7 K. De'Bell, A. B. MacIsaac, I. N. Booth and J. P. Whitehead, *Phys. Rev. B: Condens. Matter Mater. Phys.*, 1997, **55**, 15108–15118.
8 S. Prakash and C. L. Henley, *Phys. Rev. B: Condens. Matter Mater. Phys.*, 1990, **42**, 6574–6589.
9 P. Weiss, *J. Phys. Theor. Appl.*, 1907, **6**, 661–690.
10 A. Hubert, *Phys. Status Solidi B*, 1969, **32**, 519–534.
11 A. Aharoni, *Introduction to the Theory of Ferromagnetism*, Clarendon Press, 2000, vol. 109.
12 J. Escrig, P. Landeros, D. Altbir, E. Vogel and P. Vargas, *J. Magn. Magn. Mater.*, 2007, **308**, 233–237.
13 P. Landeros, O. J. Suarez, A. Cuchillo and P. Vargas, *Phys. Rev. B: Condens. Matter Mater. Phys.*, 2009, **79**, 024404.
14 D. Weber, D. Rüffer, A. Buchter, F. Xue, E. Russo-Averchi, R. Huber, P. Berberich, J. Arbiol, A. Fontcuberta i Morral, D. Grundler and M. Poggio, *Nano Lett.*, 2012, **12**, 6139–6144.
15 D. Rüffer, R. Huber, P. Berberich, S. Albert, E. Russo-Averchi, M. Heiss, J. Arbiol, A. Fontcuberta i Morral and D. Grundler, *Nanoscale*, 2012, **4**, 4989–4995.
16 A. Buchter, J. Nagel, D. Rüffer, F. Xue, D. P. Weber, O. F. Kieler, T. Weimann, J. Kohlmann, A. B. Zorin, E. Russo-Averchi, R. Huber, P. Berberich, A. Fontcuberta i Morral, M. Kemmler, R. Kleiner, D. Koelle, D. Grundler and M. Poggio, *Phys. Rev. Lett.*, 2013, **111**, 067202.
17 A. Buchter, R. Wölbing, M. Wyss, O. F. Kieler, T. Weimann, J. Kohlmann, A. B. Zorin, D. Rüffer, F. Matteini, G. Tütüncüoglu, F. Heimbach, A. Kleibert, A. Fontcuberta i Morral, D. Grundler, R. Kleiner, D. Koelle and M. Poggio, *Phys. Rev. B: Condens. Matter Mater. Phys.*, 2015, **92**, 214432.
18 M. Wyss, A. Mehlin, B. Gross, A. Buchter, A. Farhan, M. Buzzi, A. Kleibert, G. Tütüncüoglu, F. Heimbach, A. Fontcuberta i Morral, D. Grundler and M. Poggio, *Phys. Rev. B: Condens. Matter Mater. Phys.*, 2017, **96**, 024423.
19 H. D. Salinas, J. Restrepo and Ò. Iglesias, *Sci. Rep.*, 2018, **8**, 10275.
20 I. Stanković, M. Dašić and R. Messina, *Soft Matter*, 2016, **12**, 3056–3065.
21 R. Streubel, P. Fischer, F. Kronast, V. P. Kravchuk, D. D. Sheka, Y. Gaididei, O. G. Schmidt and D. Makarov, *J. Phys. D: Appl. Phys.*, 2016, **49**, 363001.
22 M. Yan, C. Andreas, A. Kákay, F. García-Sánchez and R. Hertel, *Appl. Phys. Lett.*, 2011, **99**, 122505.
23 A. P. Chen, N. A. Usov, J. M. Blanco and J. Gonzalez, *J. Magn. Magn. Mater.*, 2007, **316**, e317–e319.
24 C.-R. Chang, C. M. Lee and J.-S. Yang, *Phys. Rev. B: Condens. Matter Mater. Phys.*, 1994, **50**, 6461–6464.
25 J. A. Otálora, M. Yan, H. Schultheiss, R. Hertel and A. Kákay, *Phys. Rev. Lett.*, 2016, **117**, 227203.
26 R. Messina, L. A. Khalil and I. Stanković, *Phys. Rev. E: Stat., Nonlinear, Soft Matter Phys.*, 2014, **89**, 011202.
27 J. Hernandez-Rojas, D. Chakrabarti and D. J. Wales, *Phys. Chem. Chem. Phys.*, 2016, **18**, 26579–26585.
28 D. Morphew and D. Chakrabarti, *Nanoscale*, 2018, **10**, 13875–13882.
29 D. Morphew and D. Chakrabarti, *Nanoscale*, 2015, **7**, 8343–8350.

30 A. Kuzyk, R. Schreiber, Z. Fan, G. Pardatscher, E.-M. Roller, A. Hogele, F. C. Simmel, A. O. Govorov and T. Liedl, *Nature*, 2012, **483**, 311–314.

31 Y. Zhang, F. Lu, K. G. Yager, D. van der Lelie and O. Gang, *Nat. Nanotechnol.*, 2013, **8**, 865–872.

32 Y. Zhou and T. Shimizu, *Chem. Mater.*, 2008, **20**, 625–633.

33 M. A. Correa-Duarte, M. Grzelczak, V. Salgueiriño Maceira, M. Giersig, L. M. Liz-Marzán, M. Farle, K. Sierazdki and R. Diaz, *J. Phys. Chem. B*, 2005, **109**, 19060–19063.

34 X. Liu, I. Marangon, G. Melinte, C. Wilhelm, C. Ménard-Moyon, B. P. Pichon, O. Ersen, K. Aubertin, W. Baaziz, C. Pham-Huu, S. Bégin-Colin, A. Bianco, F. Gazeau and D. Bégin, *ACS Nano*, 2014, **8**, 11290–11304.

35 J. Yan, M. Bloom, S. C. Bae, E. Luijten and S. Granick, *Nature*, 2012, **491**, 578–581.

36 D. Zerrouki, J. Baudry, D. Pine, P. Chaikin and J. Bibette, *Nature*, 2008, **455**, 380–382.

37 M. Chen, J. Kim, J. Liu, H. Fan and S. Sun, *J. Am. Chem. Soc.*, 2006, **128**, 7132–7133.

38 J. L. C. Huaman, S. Fukao, K. Shinoda and B. Jeyadevan, *CrystEngComm*, 2011, **13**, 3364–3369.

39 G. Singh, H. Chan, A. Baskin, E. Gelman, N. Repnin, P. Král and R. Klajn, *Science*, 2014, **345**, 1149–1153.

40 S. Mehdizadeh Taheri, M. Michaelis, T. Friedrich, B. Förster, M. Drechsler, F. M. Römer, P. Bösecke, T. Narayanan, B. Weber, I. Rehberg, S. Rosenfeldt and S. Förster, *Proc. Natl. Acad. Sci. U. S. A.*, 2015, **112**, 14484–14489.

41 H.-B. Sun and S. Kawata, *NMR 3D Analysis Photopolymerization*, Springer, 2004, pp. 169–273.

42 Y.-Y. Cao, N. Takeyasu, T. Tanaka, X.-M. Duan and S. Kawata, *Small*, 2009, **5**, 1144–1148.

43 G. Williams, M. Hunt, B. Boehm, A. May, M. Taverne, D. Ho, S. Giblin, D. Read, J. Rarity, R. Allenspach and S. Ladak, *Nano Res.*, 2018, **11**, 845–854.

44 L. Bécu, M. Basler, M. L. Kulić and I. M. Kulić, *Eur. Phys. J. E: Soft Matter Biol. Phys.*, 2017, **40**, 107.

45 X.-M. Lin and A. C. Samia, *J. Magn. Magn. Mater.*, 2006, **305**, 100–109.

46 S. Sacanna, L. Rossi and D. J. Pine, *J. Am. Chem. Soc.*, 2012, **134**, 6112–6115.

47 W. Lowrie, *Fundamentals of geophysics*, Cambridge university press, 2007.

48 C.-L. Fang, K. Qian, J. Zhu, S. Wang, X. Lv and S.-H. Yu, *Nanotechnology*, 2008, **19**, 125601.

49 Y. Min, M. Akbulut, K. Kristiansen, Y. Golan and J. Israelachvili, *Nat. Mater.*, 2008, **7**, 527EP-.

50 W. H. Stockmayer, *J. Chem. Phys.*, 1941, **9**, 398–402.

51 M. A. Miller and D. J. Wales, *J. Phys. Chem. B*, 2005, **109**, 23109–23112.

52 A. Baskin, W.-Y. Lo and P. Král, *ACS Nano*, 2012, **6**, 6083–6090.

53 A.-P. Hynninen and M. Dijkstra, *Phys. Rev. Lett.*, 2005, **94**, 138303.

54 S. Plimpton, *J. Comput. Phys.*, 1995, **117**, 1–19.

55 R. Barrett, M. W. Berry, T. F. Chan, J. Demmel, J. Donato, J. Dongarra, V. Eijkhout, R. Pozo, C. Romine and H. Van der Vorst, *Templates for the solution of linear systems: building blocks for iterative methods*, Siam, 1994, vol. 43.

56 A. Concha, D. Aguayo and P. Mellado, *Phys. Rev. Lett.*, 2018, **120**, 157202.

57 D. Wood, C. Santangelo and A. Dinsmore, *Soft Matter*, 2013, **9**, 10016–10024.

58 D. Vella, E. du Pontavice, C. L. Hall and A. Goriely, *Proc. R. Soc. London, Ser. A*, 2013, **470**, 20130609.

59 A. Grzybowski and A. Bróadka, *Mol. Phys.*, 2003, **101**, 1079–1088.

60 J. G. Donaldson, P. Linse and S. S. Kantorovich, *Nanoscale*, 2017, **9**, 6448–6462.

61 J. G. Donaldson and S. S. Kantorovich, *Nanoscale*, 2015, **7**, 3217–3228.

62 R. Tao and J. M. Sun, *Phys. Rev. Lett.*, 1991, **67**, 398–401.

63 E. Feldtkeller, *IEEE Trans. Magn.*, 2017, **53**, 1–8.

64 J. A. Otálora, J. A. López-López, P. Vargas and P. Landeros, *Appl. Phys. Lett.*, 2012, **100**, 072407.

65 J. A. Otálora, A. Kákay, J. Lindner, H. Schultheiss, A. Thomas, J. Fassbender and K. Nielsch, *Phys. Rev. B: Condens. Matter Mater. Phys.*, 2018, **98**, 014403.

Nanoscale

CORRECTION

View Article Online
View Journal | View Issue

Cite this: *Nanoscale*, 2019, **11**, 2536

Correction: A platform for nanomagnetism – assembled ferromagnetic and antiferromagnetic dipolar tubes

Igor Stanković,*[a] Miljan Dašić,[a] Jorge A. Otálora[b] and Carlos García[c]

DOI: 10.1039/c9nr90017a

rsc.li/nanoscale

Correction for 'A platform for nanomagnetism – assembled ferromagnetic and antiferromagnetic dipolar tubes' by Igor Stanković *et al.*, *Nanoscale*, 2019, DOI: 10.1039/c8nr06936k.

The authors of this manuscript have noticed that the affiliations for Jorge A. Otálora and Carlos García were listed incorrectly in the original publication. A corrected affiliation list has therefore been provided with this correction.

The Royal Society of Chemistry apologises for these errors and any consequent inconvenience to authors and readers.

[a]*Scientific Computing Laboratory, Center for the Study of Complex Systems, Institute of Physics Belgrade, University of Belgrade, 11080 Belgrade, Serbia. E-mail: igor.stankovic@ipb.ac.rs*

[b]*Institute for Metallic Materials at the Leibniz Institute for Solid State and Materials Research, IFW, 01069 Dresden, Germany*

[c]*Departamento de Física & Centro Científico Tecnológico de Valparaíso-CCTVal, Universidad Técnica Federico Santa María, Av. España 1680, Casilla 110-V, Valparaíso, Chile*